Nanoscale Advances

Accepted Manuscript

This article can be cited before page numbers have been issued, to do this please use: E. A. Kamoun, A. T. Mosleh, H. A. Hossni, T. A. Yousef, N. A.M. Ragab, H. Y. Zahran, V. Ganesh, M. H. Ahmed, I. S. Yahia and S. A. Fareed, *Nanoscale Adv.*, 2026, DOI: 10.1039/D6NA00277C.

ROYAL SOCIETY OF CHEMISTRY

rsc.li/nanoscale-advances

View Article Online
DOI: 10.1039/D6NA00277C

Fabrication of novel nitrogen-doped δ-Al_2O_3 NPs: Characterization and performance evaluation for electrocatalytic degradation of organic dyes

Elbadawy A. Kamoun[1*], Ahmed T. Mosleh[2], Habiba A. Hossni[2], Tarek A. Yousef[3], Nourhan A.M Ragab[2], Heba Y. Zahran[4], V. Ganesh[4], Mohamed Hafez[5,6], Ibrahim S. Yahia[4*], Shereef A. Fareed[7]

[1]*Department of Chemistry, College of Science, King Faisal University, Al-Ahsa 31982, Saudi Arabia.*
[2]*Nanotechnology Section., Egyptian Company for Carbon Materials, El-Sheraton/El-Nozha, Cairo, Egypt.*
[3]*Chemistry Department, College of Science, Imam Mohammad Ibn Saud Islamic University (IMSIU), Riyadh 11623, Saudi Arabia.*
[4]*Laboratory of Nano-Smart Materials for Science and Technology (LNSMST), Department of Physics, Faculty of Science, King Khalid University, P.O. Box 9004, Abha, Saudi Arabia.*
[5]*Faculty of Engineering and Quantity Surveying INTI, IU, Universi, Nilai, Malaysia.*
[6]*Faculty of Management, Shinawatra University, Pathum Thani Thailand.*
[7]*National Research Institute of Astronomy and Geophysics (NRIAG), Helwan 11421, Cairo, Egypt.*

**Corresponding authors: E.A. Kamoun, E-mail: ekamoun@kfu.edu.sa, Tel: 00201283320302, and I.S. Yahia. E-mail: dr_isyahia@yahoo.com.*

Abstract

This work constructs novel N-doped δ-Al_2O_3 nanoparticles (NAO) based gelatin support by sol-gel/auto-combustion method. XRD analysis proved NAO NPs' tetragonal structure, which proved the delta-phase (δ) formation of Al_2O_3 NPs. SEM micrographs of NAO NPs showed an irregular shape with a rocky surface, and a grain size ranging from 34.9 to 66.6 nm. The direct energy of the band gap value of fabricated NAO-3 NPs was approximately 5.305 eV, indicating a promising response to electrocatalytic activity. NAO-3 NPs demonstrated effective electrocatalytic degradation of both *Carmine* and *Eosin Yellow* dyes. Fabricated NAO-3 NPs catalyst achieved degradation efficiency 96.3% (0.28112 min^{-1}) and 97.5% (0.19828 min^{-1}) within 10 min and 12 min, respectively, in case of *Carmine* and *Eosin Yellow* dyes; respectively, while mixed dyes are degraded 98.60 %. Trapping analysis exposed that the primary species which initiate electrocatalytic degradation of *Carmine* dye is $O_2^{\bullet-}$ radical. After five cycles of electrocatalytic degradation, NAO-3 NPs' electrocatalytic performance decreases slightly to 90.5%, demonstrating NAO NPs possess an excellent stability and recyclability throughout the electrocatalytic reaction process for degradation of organic pollutants.

Keywords: *Auto-combustion; N-doped δ-Al_2O_3; DRS; Electrocatalysis; Mixed dye.*

View Article Online
DOI: 10.1039/D6NA00277C

1. Introduction

Human activity rapidly depletes freshwater due to chemical pollution, leading to socioeconomic issues, environmental degradation, and food insecurity [1]. To eradicate this pollution, scientists are searching for new approaches to fight environmental contamination [2]. In particular, synthetic dyes pose a significant risk to the production of our water supply [3]. However, wastewater treatment involves physical, biological, and chemical processes forward by analysis for dynamic control and process management of hazardous pollutants essential for safeguarding the environment against pollution [4, 5]. On the other hand, toxic pollutants in wastewater from textiles [6], printing [7], and food processing pose environmental hazards [8]. Dyes are hazardous to the environment because of their toxicity, stability, and vibrant colors [9].

Carmine dye is a naturally anionic organic dye derived from the dried corpses of female *Cocus cactus L.* insects, soluble in alkaline solutions and stable at pH values above 6 [10]. Additionally, it is commonly utilized in cosmetics. It is utilized in the natural colorant, plastic, and pharmaceutical fields and has a special role in textiles [11]. *Eosin yellow (EY)* is a water-soluble fluorescein, an anionic dye created from xanthene, used in industrial aquatic environments and applications such as painting, printing, and leather [12, 13]. However, it might lead to human genotoxicity, irritate the skin, and block protein interactions; thus, purification is an essential issue [14, 15].

Numerous techniques for treating wastewater have been investigated, including oxidation, adsorption, biodegradation, coagulation, flocculation, photodegradation, and electrocatalytic degradation, leading to either partial or complete mineralization of organic components [16, 17]. Among other methods, electrocatalysis is the basis of the advanced oxidation process (AOP). Rather, electrochemical advanced oxidation processes (EAOPs) got outstanding consideration for competent degradation of organic pollutants to reduced or inorganic substrates via generating highly active hydroxyl radicals ($^{\bullet}OH$) [18, 19]. Over the past decade, electrochemical (EC) treatment methods such as electrodeposition, electro/flotation, electrocoagulation, and electro-oxidation have generated much interest in the study because of their low cost and excellent flexibility. It is a substitute for treating industrial wastewater [20, 21].

Recently, EC oxidation has grown numerous advantages, including mild operation, environmental friendliness, selective degradation, stable long-term results, and a wide range of applications associated with electrocatalytic degradation for lowering water pollution and generating green

View Article Online
DOI: 10.1039/D6NA00277C

energy [22, 23]. Various scientific organizations have widely employed EC oxidation methods, including direct and indirect oxidation, for removing wastewater-containing dyes by enhancing the catalytic activity of catalyst materials while controlling operating conditions [24-26]. EC treatment requires active groups with sufficient oxidative qualities or electrolyte solutions supplied via various pathways, including hydroxyl radicals, sulfate radicals, and chlorine radicals, either by applying energy or using a catalyst [27, 28]. Thus, redox processes, which can degrade a range of organic compounds, including dyes, into environmentally beneficial chemicals, are subsequently facilitated by reactive oxygen species (ROS) [18, 29, 16]. Various semiconductor metal oxides with different morphologies have been explored as a sustainable solution for converting contaminants into simpler substances since their high surface charge and chemical inertness, such as Al_2O_3, CuO, TiO_2, and Fe_2O_3 [30]. This method is inexpensive and crucial for light absorption, charge transfer, and hydrogen production [31, 32]. Alumina (Al_2O_3) is an extremely important ceramic material for theoretical research and practical applications [33]. It has ideal electrical insulation, toughness, erosion and corrosion resistance, and durability [34]. Because of their accessibility and reconfigurable architecture, Al_2O_3 is being investigated as a possible material for metal oxide with high durability and dye removal rates [35, 30]. Al_2O_3 NPs play a significant role for information of energy bands and generate oxidative species, which enable them to work as an electrocatalytic degradation entity during application study [36]. Using sol-gel method, low-temperature, energy-efficient, and readily scaled-up production approaches have been reported elsewhere [37]. The sol-gel auto-combustion method is chosen due to it is economical, straightforward, and useful, resulting in a low calcination temperature and good product homogeneity [38]. Dopant elements are added to bare semiconductors to create energy between valence and conduction bands, which appropriately alters semiconductors' light-absorbing characteristics. N-doped semiconductors appear to be the most favorable dopant elements among all of them; they are active when exposed to electrocatalytic activity [39].

Numerous studies used Al_2O_3 NPs as a catalyst for adsorption of cationic dyes, underscoring their potential to alleviate water pollution, as previously studied by Manikandan et al. [40], where γ-alumina (Al_2O_3) nanoparticles were synthesized using Tween-80 and formamide. Methylene blue dye was successfully adsorbed from water by Al_2O_3 NPs, exhibiting a capacity increase ranging 490 to 2210 mg g^{-1} as starting concentration raised from 50-400 mg L^{-1} under pH 9, 10 min reaction time at 60°C [40]. For instance, *Pang et al*. stated that 97.96 % degradation efficiency for

View Article Online
DOI: 10.1039/D6NA00277C

RGO/ZnO compared to *Congo red* dye in 60 min [41]. *M. Ghozza et al*. used $Bi_{0.9}Ba_{0.1}FeO_3$ for degrading 96.5 % of Congo red dye during 4 min [42]. *Xu et al.* prepared g-C_3N_4/Fe_3O_4/AlON via hydrothermal method. Under visible-light, g-C_3N_4/Fe_3O_4/AlON exhibited significantly enhancement on degradation efficiency for methyl orange (MO) achieved 95.9 % degradation within 240 min [43].

In this study, we fabricated N-doped δ-Al_2O_3 NPs by sol-gel/auto-combustion method. At first, characterization of as-fabricated materials was assumed by XRD, FTIR, TGA, SEM, energy dispersive X-ray analysis (EDX), and diffuse reflectance spectroscopy (DRS) analyses to determine materials' crystalline nanostructures, chemical structure, surface morphologies, and compositions. Optical properties were evaluated by various analyses. Nitrogen doping is introduced as an innovative approach to modify electronic structure of Al_2O_3 NPs, effectively reducing their band gap, enhancing charge carrier mobility, and promoting electron transfer efficiency during electrocatalytic activity and stability were investigated by evaluating EC degradation of organic chemicals, *e.g*., *Carmine* and *Eosin Yellow* dyes, using novel N-doped δ-Al_2O_3 NPs.

2.Materials and methods

2.1. Materials

Aluminum acetate ($C_2H_5O_4Al$, 99%), Gelatin (purity: 98%). *Carmine* dye ($C_{22}H_{20}O_{13}$) and *Eosin Yellow* (EY) ($C_{20}H_6Br_4Na_2O_5$), Sodium chloride (NaCl, purity 98), sodium nitrate ($NaNO_3$, purity 98%), ethylene diamine tetra acetic acid (EDTA) ($C_{10}H_{16}N_2O_8$, purity 98%), ascorbic acid ($C_6H_8O_6$, purity 99%), isopropyl alcohol (C_3H_8O, purity 99%) were gotten from Sigma-Aldrich, Germany. Distilled water (DW) was used for further experiments.

2.2. Fabrication of N-Al_2O_3 NPs

N-doped δ-Al_2O_3 NPs were synthesized by sol-gel/auto-combustion method [44]. First, 5 g of aluminum acetate was taken, followed by adding gelatin with different ratios (0.001, 0.01, 0.1, 0.25, 0.5, 1, 5, and 10) g as a nitrogen source to create N- doped δ-Al_2O_3, where sample codes are presented as (NAO-1, NAO-2, NAO-3, NAO-4, NAO-5, NAO-6, and NAO-7, NAO-8), respectively based on the incorporated gelatin content. 30 mL of distilled water is added and mixed well at 25 ^oC with continuous stirring to get a homogeneous solution forming a gel. Then, the gel was dried at 80°C in an oven for 12 h and calcined for 2h at 850°C to produce N-doped δ-Al_2O_3 NPs, as shown in Fig. 1(a).

View Article Online
DOI: 10.1039/D6NA00277C

The reaction mechanism for the Synthesis of N-doped δ-Al_2O_3 NPs is as follows:

$$2Al(CH_3COO)_3 + Gelatin \xrightarrow{\Delta} N-doped\ \delta-Al_2O_3 + nCO_2 + nH_2O + nNH_3 \quad (1)$$

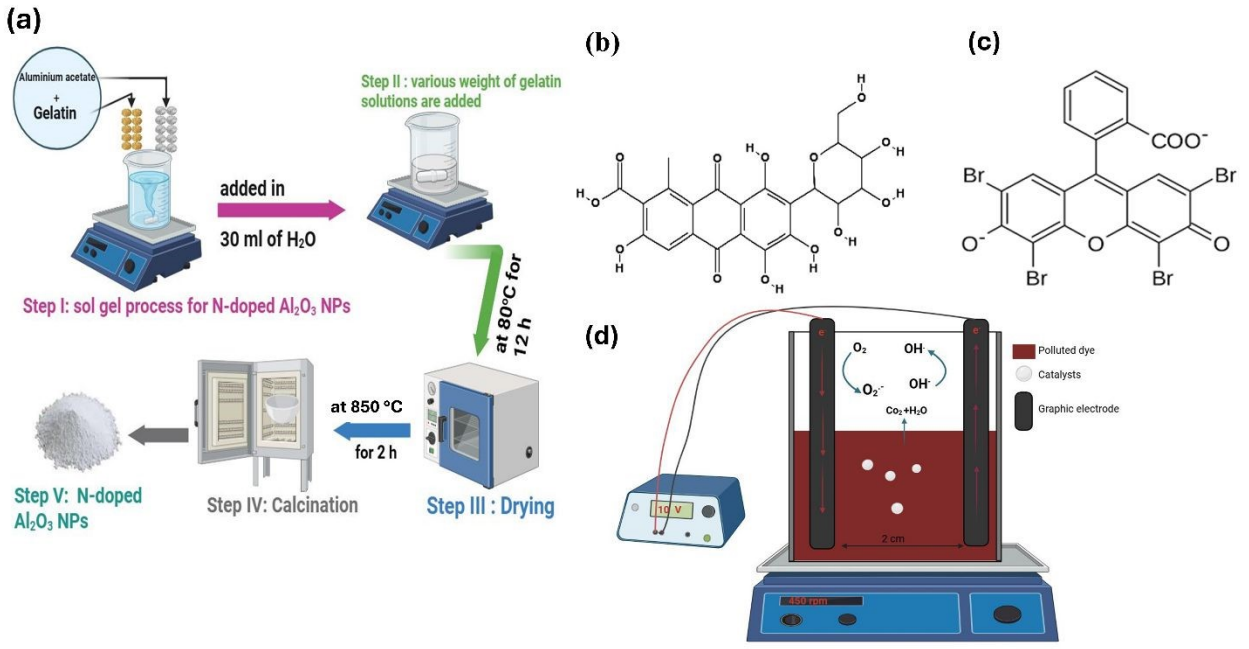

Fig. 1 (a) Schematic diagram of fabrication of N-doped δ-Al_2O_3, **(b)** structure of *Carmine dye*, **(c)** *Eosin yellow* dye, and (**d**) Schematic diagram of used electrocatalytic cell.

2.3. Study of electrocatalytic degradation

Electrocatalytic degradation was employed in a single electrochemical cell at an ambient temperature. Two parallel graphite electrodes with an area of 1.40 mm^2 and a distance between cathode and anode is 2 cm, fixed in the applied cell, and solution conductivity is 0.063 S/m. 200 mL of *Carmine* (100 ppm) and *Eosin Yellow* (50 ppm) dye were merged with 0.05 g/L of NAO NPs catalyst at pH = 7, and 10 mL of 1M NaCl was then added to improve conductivity. *Carmine* and *EY* dyes were degraded using a regulated DC power supply. The applied potential (DC) remains at 10V during the electrochemical process, as shown in Fig. 1(d). The voltage operates the electrochemical process and particle repolarization at the electrode. The particle at the electrode becomes more repolarized as the voltage rises. *Carmine* and *EY* dyes' electrochemical reaction changes; thus, the degradation effect improves, and the reaction speed increases [45]. The samples were taken at specific times using similar absorption wavelengths for the UV-Vis spectrophotometry analysis. To determine absorbance percentage of dye degradation using following equation [46]:

View Article Online
DOI: 10.1039/D6NA00277C

$$Degradation\,\% = \frac{A_o - A}{A_o} \times 100, \qquad (2)$$

where A_o is initial absorbance of dyes, and A is absorbance at different times.

2.4. Instrumental devices

XRD (Shimadzu LabX-XRD-6000, Japan) detects patterns of films created in reflection mode by *CuK* (radiation) (λ = 1.5406 Å) with a scanning rate of 0.02 degrees/s; it was used to determine the crystalline structure of prepared materials. XRD tube worked at 10-80 degrees at 30 kV and 30 mA of current. XRD peaks were indexed by *X'pert High Score* software.

FT-IR (Nicolet IS50, Thermo Electron Corporation, Waltham, MA) was used to detect chemical composition and functional groups of prepared samples at 4000– 400 cm^{-1}.

The microstructure of composites was examined at 30 kV by (SEM) (JSM-6360, JOEL, Japan), with energy-dispersive X-ray spectroscopy (EDX), elemental mapping technique was operated to identify elemental composition analysis, where *Image j* program was utilized for determining grain size.

HR-TEM model (Jeol, JEM-2100 plus, Japan) was utilized to examine the nanocomposite and photocatalysts at an accelerating voltage of 200 kV.

Spectrophotometer (Shimadzu UV-3600 model UV-Vis DRS, Japan) was established for optical scattered reflectance measurements in λ (200–800 nm). Combining sphere connection with KBr served as the reference material.

Surface area analysis was performed by N_2 adsorption–desorption measurement of sample coded NAO-3 NPs at 77K by BET surface area and pore size distribution analyzer (BELSORP-miniX 10115, Microtrac, Inc., USA).

UV–Vis single-beam spectrophotometer (LISCO-GmbH, Germany) was employed to follow degradation process in ambient environment.

3. Results and discussion

3.1. XRD analysis

Figure 2(a) presents diffraction patterns obtained by XRD analysis of N-doped δ-Al_2O_3 NPs crystalline structure, which proves the delta-phase (δ) of δ-Al_2O_3 as a pattern, which is matching with standard card No. (*ICDD 00-016-0394*) [47]. XRD patterns show crystallographic plane at 2θ angles □ 22.8°, 25.17°, 26.11°, 29.04°, 31.20°, 33.19°, 35.86°, 38.42°, 40.22°, 45.70°, 49.99°, 57.19°, and 62.30°, conforming to crystal planes (1 1 4), (1 1 5), (2 1 3), (1 0 7), (1 1 7), (2 2 2), (3 2 1), (3 1 4), (2 2 6), (4 0 0), (2 2 10), (2 2 12), and (4 0 10); respectively. N-doped δ-Al_2O_3 NPs

View Article Online
DOI: 10.1039/D6NA00277C

demonstrates tetragonal structure with dimensions a = b = 7.944 Å, c = 23.120 Å, α =β = γ = 90°. While Al_2O_3 NPs have another phase called gamma (γ) γ -Al_2O_3, as a pattern that matches the standard card No. (*ICDD 10-0425*) with a clear cubic structure [48]. Absence of additional peaks indicates high purity of N-doped δ-Al_2O_3 NPs sample. The peaks further verify that both have the same crystal structure and that the precursor to the fuel ratio is irrelevant to the crystal structure. Despite not affecting the structure, the fuel quantity influences the unit cell's volume [41]. *Equation (3)* shows that *Debye-Scherrer* formula, which was sourced to verify average crystallite size:

$$D = \frac{k\,\lambda}{\beta\, Cos\,\theta}, \quad \textbf{(3)}$$

Where, λ is wavelength in nanometers, β is width peak at half maximum, θ is *Bragg's* angle (degree), D is crystallite size, and k is *Scherer*'s constant (k = 0.9).

$$\delta = 1/D^2, \quad \textbf{(4)}$$

$$\varepsilon = \frac{\beta\, Cos\,\theta}{4}, \quad \textbf{(5)}$$

In the meantime, *Eqs. (4 and 5)* are used to estimate micro-strain (ε) and average dislocation density (δ) for N-doped δ-Al_2O_3 NPs [49].

From Fig. 2(a), peak is narrow, indicating the remarkable crystallinity of NAO NPs. The lattice structure of tetragonal structure can be evaluated using *Eq. (6)*, as shown in Table. 1.

$$\frac{1}{d^2} = \frac{h^2+k^2}{a^2} + \frac{l^2}{c^2}, \quad \textbf{(6)}$$

Where, (D) is size of crystallite NAO NPs using X-ray diffraction, (θ) is *Bragg's* angle, (λ) is wavelength of X-ray radiation (1.5406 Å), and (β) for full width at half maximum (FWHM) of diffraction peak. Incorporating gelatin in preparation of NAO nanoparticles notably influences their structural characteristics. As a polymerization agent and growth terminator, gelatin is crucial in reducing particle size to around 20 nm. XRD analysis reveals that the presence of gelatin affects crystallite size and significantly enhances the crystallinity of NAO NPs, resulting in more uniformly distributed and well-defined structures.

View Article Online
DOI: 10.1039/D6NA00277C

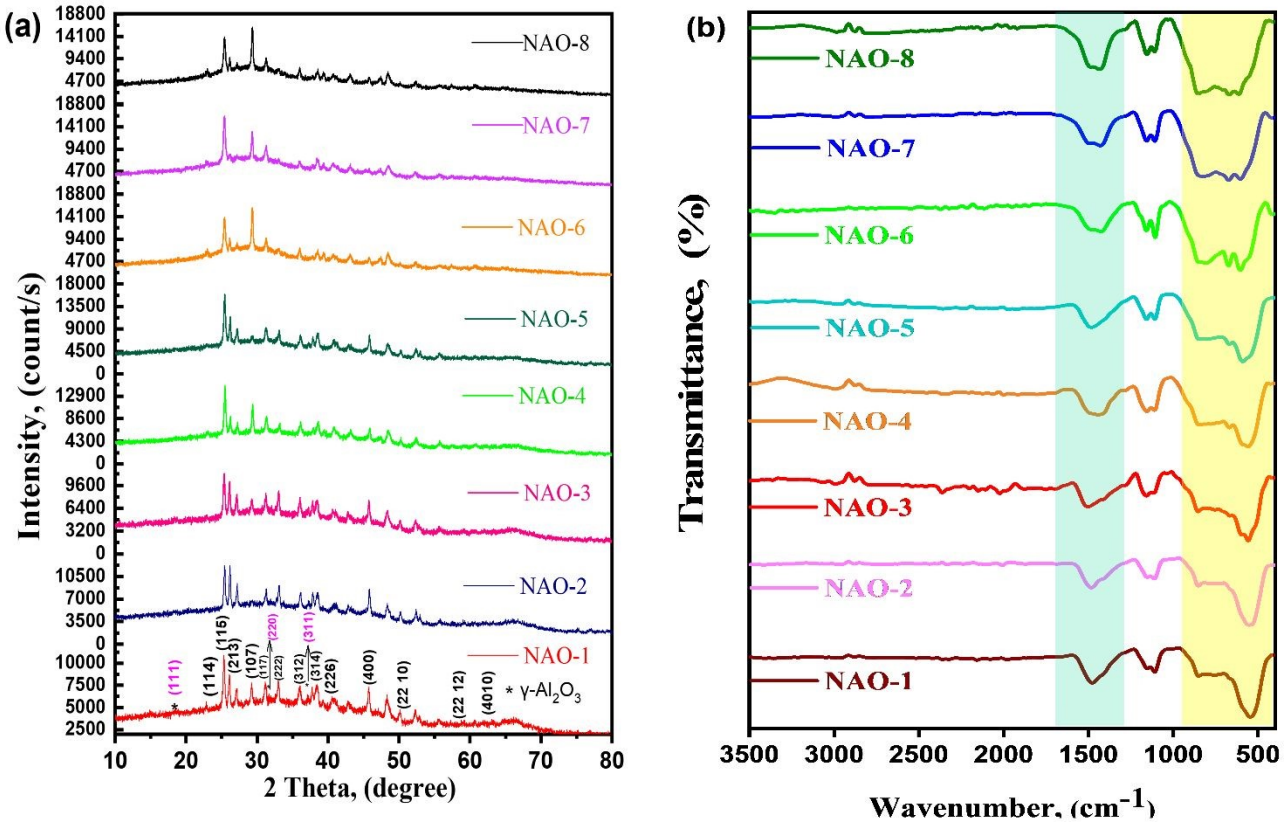

Fig. 2 (a) XRD spectra for N-doped δ-Al_2O_3 NPs, and **(b)** FTIR spectrum of N-doped δ-Al_2O_3 NPs.

Table 1: Dislocation density and average crystal size, micro-strain, and lattice structure values were calculated using XRD spectra for NAO NPs.

Samples	Average D, (nm)	(δ), (nm)$^{-2}$	Lattice strain	d- spacing, (Å)	a =b, (Å)	c, (Å)	V, (Å^3)
NAO-1	21.38	2.829E-03	1.744E-03	1.9843	7.937	23.179	1460.28
NAO-2	22.69	2.783E-03	1.768E-03	1.9803	7.921	23.155	1452.88
NAO-3	21.25	2.910E-03	1.770E-03	1.9830	7.932	23.159	1456.72
NAO-4	22.05	2.556E-03	1.669E-03	1.9796	7.798	23.119	1405.84
NAO-5	19.76	3.366E-03	1.917E-03	1.9800	7.920	23.123	1450.42
NAO-6	21.30	2.843E-03	1.750E-03	1.9898	7.959	23.115	1464.24
NAO-7	20.311	2.858E-03	1.798E-03	1.9799	7.919	23.119	1449.81
NAO-8	21.01	3.184E-03	1.817E-03	1.9810	7.924	23.102	1450.57

3.2.FTIR analysis

View Article Online
DOI: 10.1039/D6NA00277C

FT-IR spectroscopy is appropriate for evaluating absorption of IR radiation by sample. Relationship between absorption bands (vibrational bands) and chemical substance in sample, is included by infrared spectrum analysis [50]. FTIR spectra were employed to detect functional groups of N-doped δ-Al_2O_3 in different ratios of gelatin. FTIR spectra of observed N-doped δ-Al_2O_3 NPs, as shown in Fig. 2(b). N-H stretching is detected at ν 3347 cm^{-1} [51]. The gelatin absorption bands are found in the infrared spectra of amide band region [52]. The bands at ν 1687 cm^{-1} area show the existence of C=O bond [53]. The C=O stretching mode corresponds to band at ν 1153 and 1106 cm^{-1} [54]. While, peaks at ν 545 cm^{-1} and 753 cm^{-1} are assigned to aluminum oxide stretching [35]. Peaks at ν 545 cm^{-1} are shifted to a higher ν of 611 $cm^{-1,}$ and intensity of these peaks is reduced as increasing gelatin.

3.3.TGA analysis

TGA thermograph is frequently used to investigate the residual mass at higher temperatures and the thermal stability of nanocomposites. Figures 3(a–h) illustrate TG, DSC, and DTG curves of sample coded NAO NPs. The sample's mass decreased as temperature rose from RT- 550^oC, according to TG and DSC data. The sample's moisture, humidity or adsorbed water is lost between 25–100 ^oC, and the weight of NAO NPs is gradually decreases between 12–18% at 550 ^oC [55]. The weight loss changes become more obvious as gelatin amount increases during synthesis step [56]. DTG curve shows that there is little change in the heat of exotherm between room temperature and 350 ^oC. Water evaporation causes a tiny endothermic thermometric peak at 200^oC. The breakdown reaction's primary temperature range is 400–500 ^oC, where there is a noticeable endothermic peak [57]. The most obvious mass change occurred at 404 ^oC. Thereafter, the rate of mass change gradually decreased with temperature.

View Article Online
DOI: 10.1039/D6NA00277C

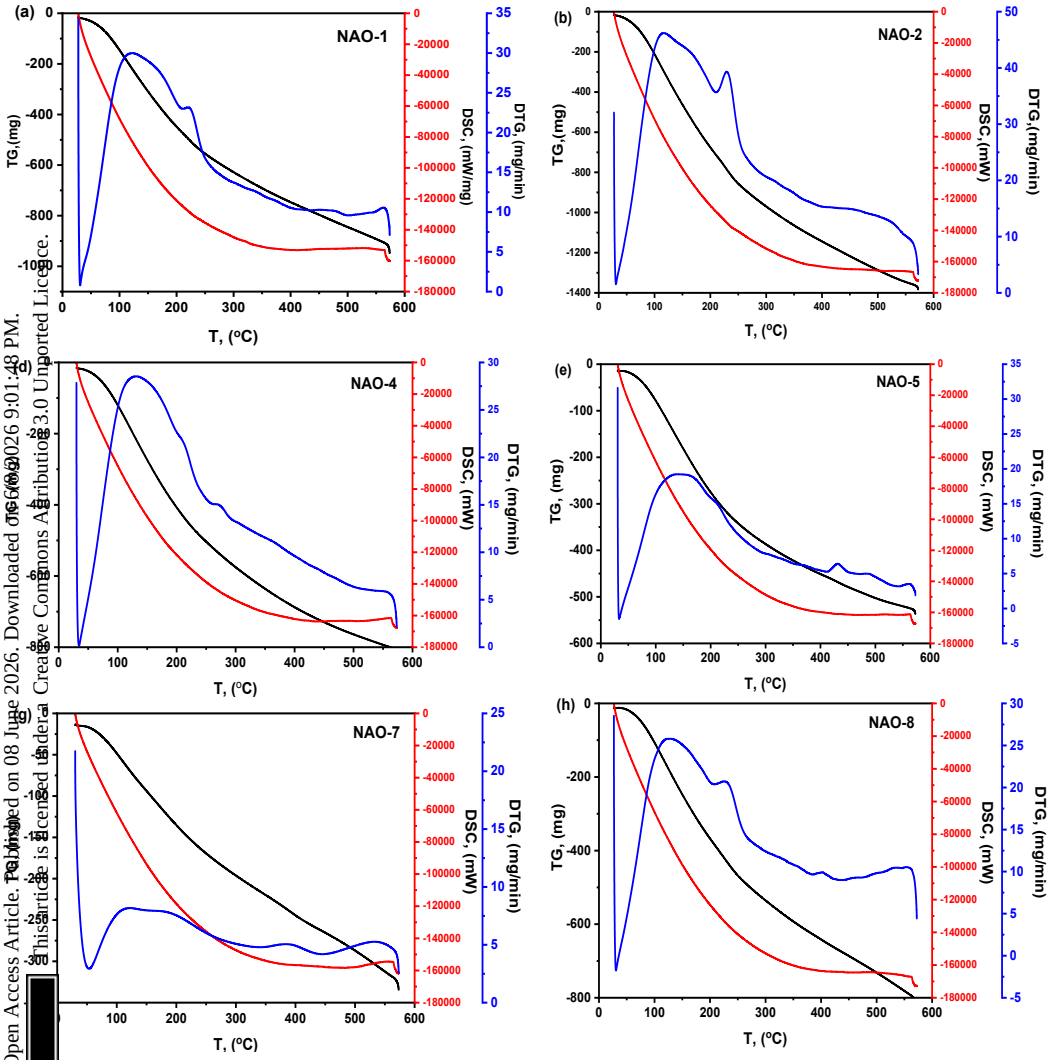

Fig. 3 TGA, DSC, and DTG thermographs of N-doped δ-Al_2O_3 NPs.

3.4. FE-SEM and EDX investigation

FE-SEM shows surface morphological alterations and microstructure of NAO NPs samples. Figures 4(a–h) illustrate that crystalline structures are semi-spherical, and irregular shapes that come in varied sizes and shapes. Also, visible in images are clusters of many NPs [58]. Tadic et al., have investigated the cause of variations in particle shape and cluster formation in relation to magnetic characteristics of NPs that influence particles' size and shape [59]. Figures 4(a`-h`) show that NAO NPs size distribution are ranging from 34.9–66.6 nm. Figure 5(a) shows energy dispersive spectroscopy (EDX) of prepared NAO NPs. The visible peaks are found for Al, O, and N without any impurities of element. Furthermore, a trace amount of element Au has also been

View Article Online
DOI: 10.1039/D6NA00277C

found, since the sample was coated with gold, during samples preparation before FE-SEM scan and investigation to make it conductive [60]. Based on EDX spectra, the weight percentages of Al, O, and N are 27.41, 56.02, and 16.57 %, respectively. Whereas Figures 5(b-e) display elemental mapping of NAONPs which confirm homogenous distribution of element.

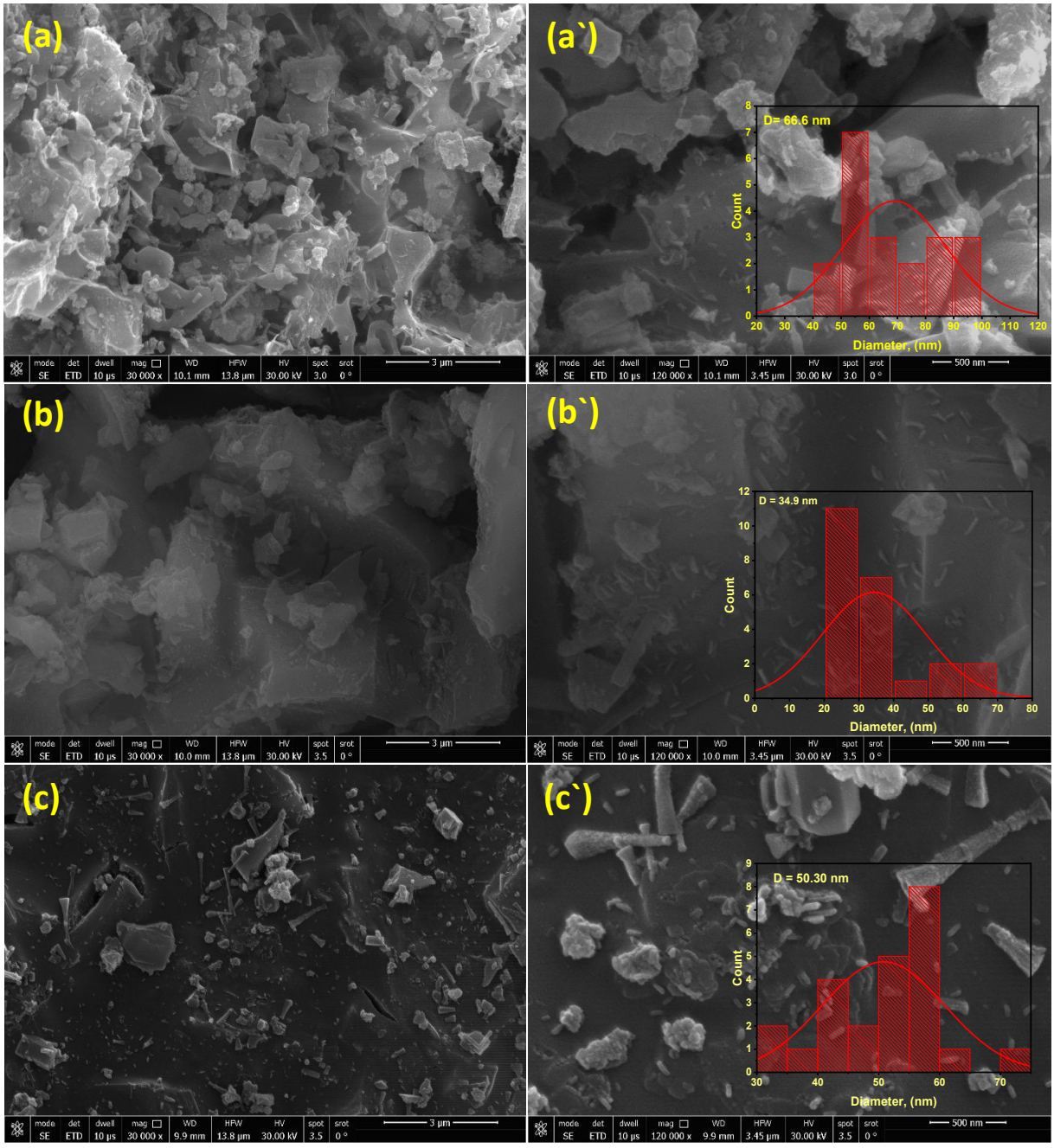

View Article Online
DOI: 10.1039/D6NA00277C

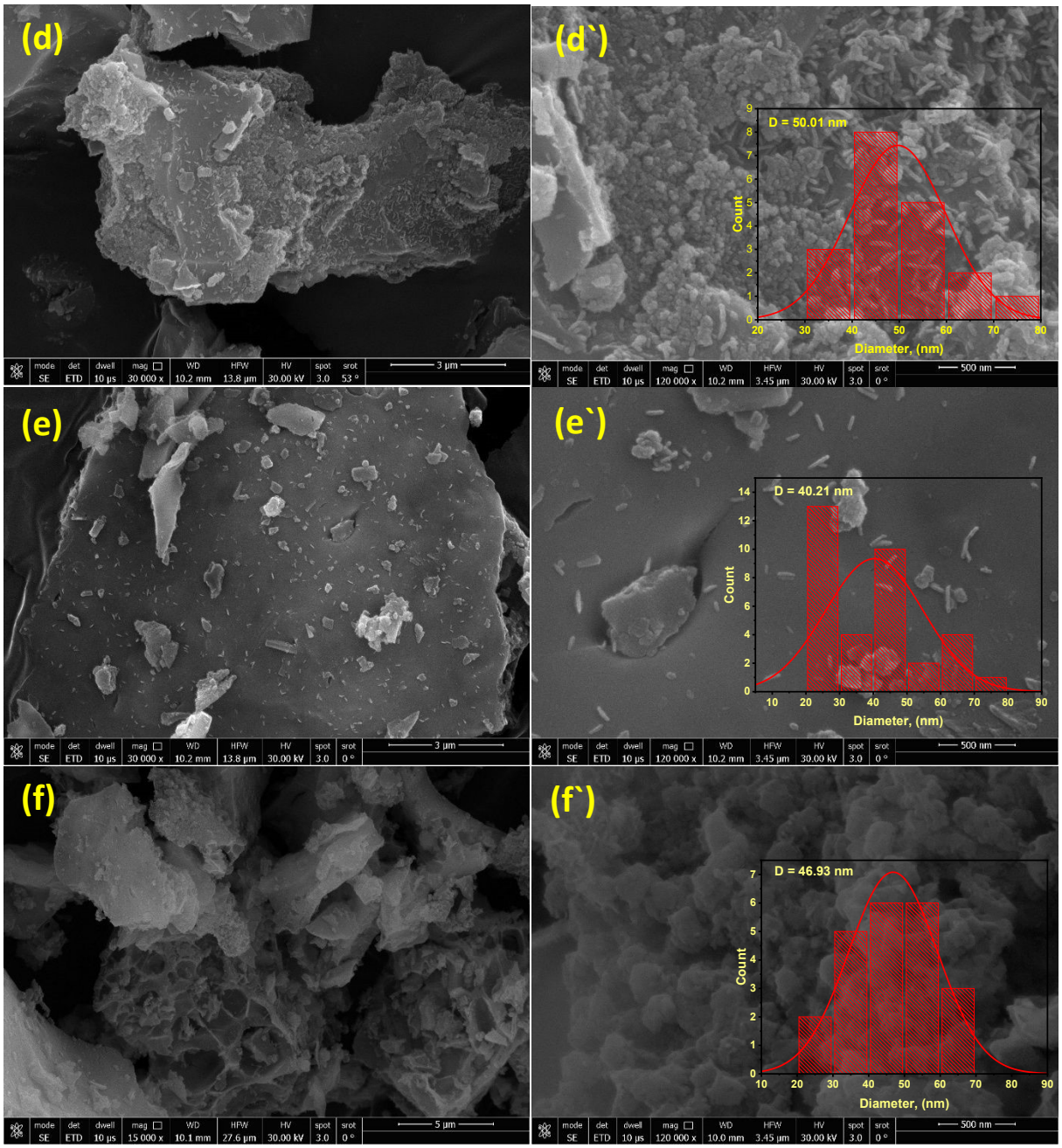

View Article Online
DOI: 10.1039/D6NA00277C

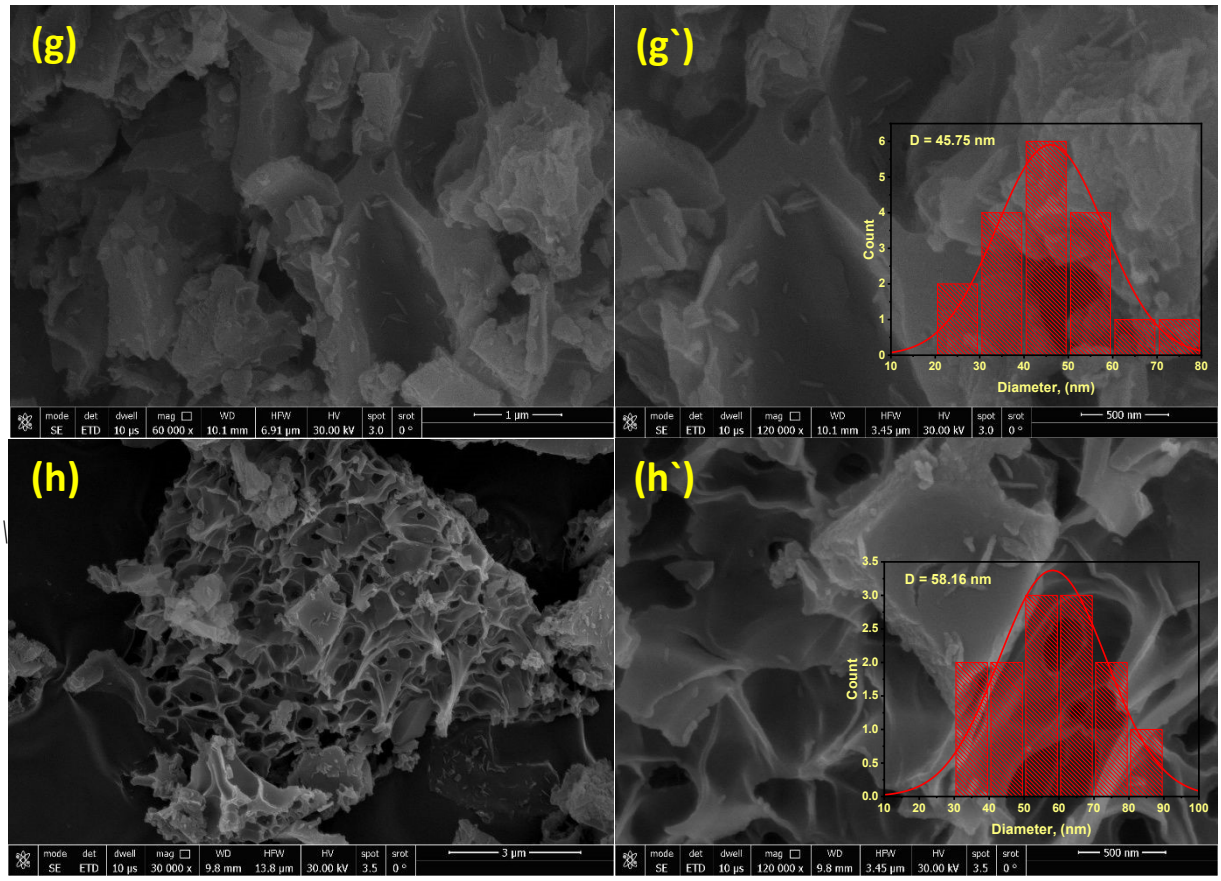

Fig. 4: (a-h) SEM micrographs of N-doped δ-Al_2O_3 NPs, *all samples were imaged at different magnification (3µm, 500 nm and applied voltage 30 KV).*

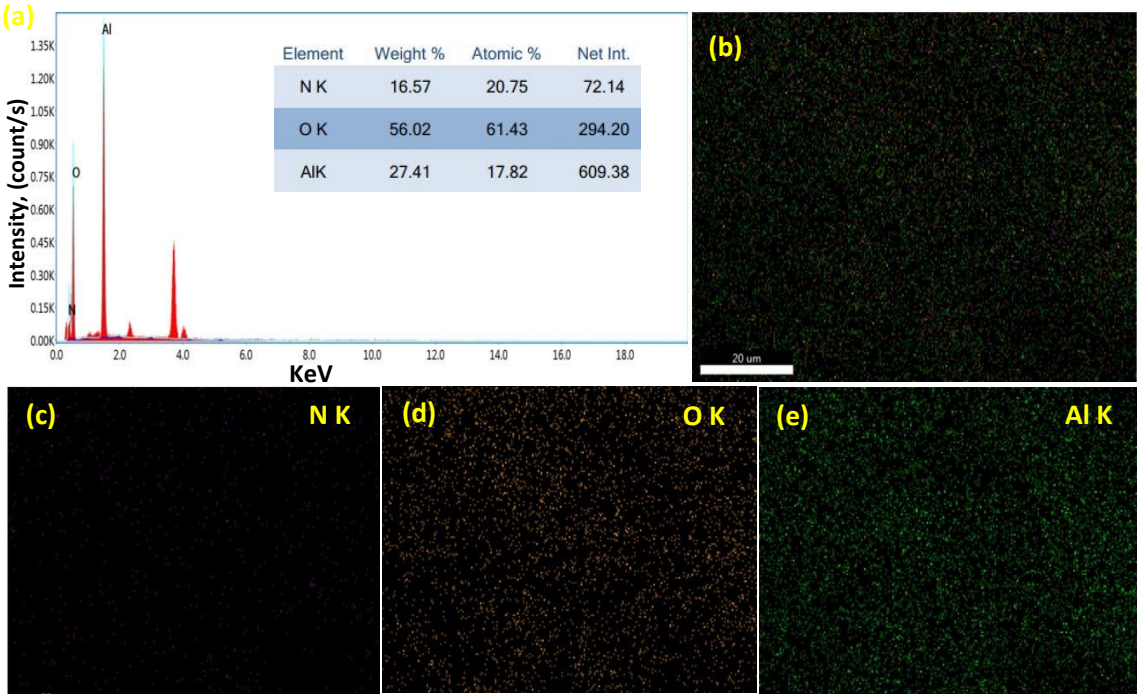

Fig. 5: (a) EDX of NAO-3 NPs, **(b- e)** elemental mapping of N-doped δ-Al_2O_3 NPs.

View Article Online
DOI: 10.1039/D6NA00277C

3.5. HR-TEM analysis

The morphology of NAO-8 NPs is visually represented by TEM investigation in Figures 6(a, b). The iimages show that NAO-8 NPs have an irregular layered structure with certain mesoporous properties and are dispersed randomly. This observation is similar to results reported by Manikandan et al.[40]. Additionally, images also show that prepared NAO-8 NPs have uniformly sized particles and are still less agglomerated. Furthermore, the crystalline interplanar lattice spacing of 0.35 nm precisely matches (115) crystal plane of Al_2O_3 NPs, as shown in Figure 6(c) of HR-TEM image. As shown in Figures 7(d), the average particle size of NAO-8 NPs is 18 nm.

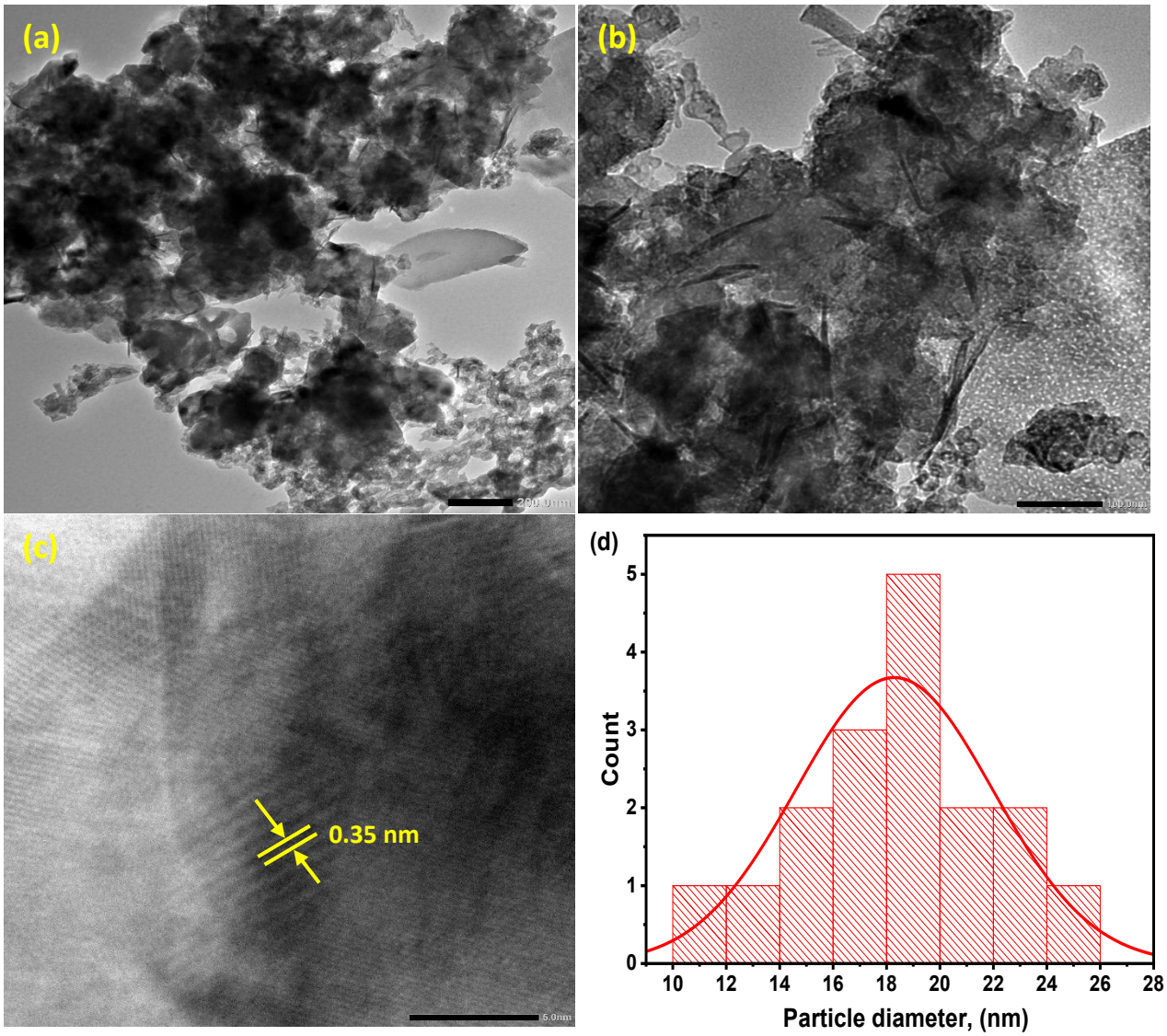

Fig. 6 (a, b) TEM image of N-doped δ-Al_2O_3 NPs, (c) HR-TEM, and (d) particle distribution histogram.

View Article Online
DOI: 10.1039/D6NA00277C

3.6. UV -Vis DRS analysis

DRS was done to obtain some information on optical properties of N-doped δ-Al_2O_3 NPs. Fig. 7(a) demonstrates UV-Vis DRS analysis of N-doped δ-Al_2O_3 NPs samples. DRS analysis was employed to specify samples' energy band gap and certain λ edge's absorption wavelength. *Kubelka–Munk* function *F(R)*, is relative to absorption coefficient of NAO NPs and was calculated from *Eq. (7)* [61]*:*

$$F(R) = \frac{(1-R)^2}{2R}, \quad \textbf{(7)}$$

Where, *R* in function is reflectance of NAO NPs. Results show absorption of fabricated NAO NPs in λ 450–200 nm range. As shown in Fig. 8(a), a noticeable weak and wide absorption peak was observed at 221 nm in all prepared N-doped δ-Al_2O_3 NPs samples because of the four-fold coordinated surface's charge inter-band transition O^{2-} valance band to Al^{3+} conduction band [62]. The absorption peak experiences a red shift with growing gelatin. In UV spectrum, NPs only exhibit a weak capacity to absorb light [63]. Basically, due to charge transfer transitions from O_2^- to Al^{3+}, the surface defect variations induced from oxygen and the crystal phase transformations, δ-Al_2O_3 crystalline with varied morphologies and crystalline. The absorption peak at 279 nm in Fig. 7(a) links to threefold coordinated O^{2-} anions on surface of as-fabricated N-doped δ-Al_2O_3 NPs [64]. To estimate optical energy gap of N-doped δ-Al_2O_3 NPs, *Tauc's Eq.* was used as follows [65]:

$$(\alpha h\nu)^n = A(h\nu - E_g), \quad \textbf{(8)}$$

Where, hυ, α, A, and E_g are incident light frequency, absorption coefficient, an energy-independent constant, and band gap energy, correspondingly. Furthermore, value of (*n*) is determined by the kind of optical transitions in semiconductors. It is set to 1/2 for a direct and 2 for an indirect bandgap semiconductor. Figures 7(b) reveals direct bandgap. The computed E_g values of N-doped δ-Al_2O_3 NPs with varying gelatin concentrations (Table 2). Direct band gap energy value of fabricated NAO-3 is approximately 5.305 eV. This observation is similar to results reported by Akouibaa *et al*. [66], where the material exhibits semiconductor characteristics despite its insulating behavior because of surface defects that add energy levels to band gap, making it easier to generate charge carriers and providing them with possible uses in the catalytic application [67, 68].

View Article Online
DOI: 10.1039/D6NA00277C

Table 2: Direct bandgaps correspond for N-doped δ-Al_2O_3 NPs.

Samples	E_g direct, (eV)	Electrocatalytic degradation of *Carmine dye*		Electrocatalytic degradation of *Eosin yellow* dye	
		Degradation, (%)	K, (min^{-1})	Degradation, (%)	K, (min^{-1})
NAO-1	5.382	76.35	0.12515	76.61	0.07484
NAO-2	5.348	86.22	0.18242	87.85	0.11542
NAO-3	5.305	96.25	0.28112	97.50	0.19828
NAO-4	5.340	94.48	0.26653	71	0.07156
NAO-5	5.361	78.08	0.13628	89.02	0.12043
NAO-6	5.332	84.69	0.17051	87.47	0.11215
NAO-7	5.328	93.15	0.23562	48.09	0.04796
NAO-8	5.355	93.75	0.24303	51.58	0.05486

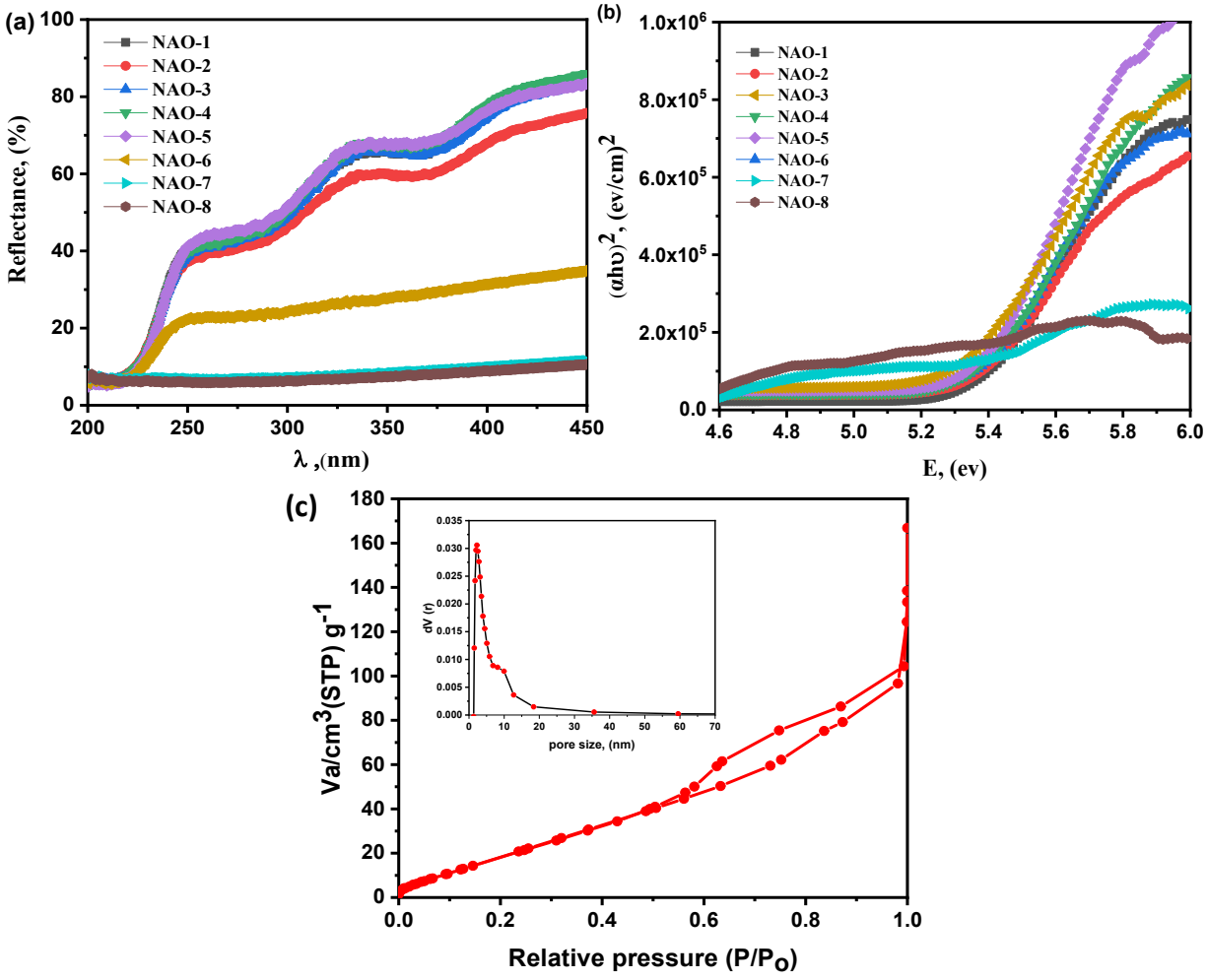

Fig. 7 (a) Reflectance spectra, **(b)** direct energy band gap of N-doped δ-Al_2O_3 NPs, and (**c**) BET analysis of NAO-3 NPs.

View Article Online
DOI: 10.1039/D6NA00277C

3.7. BET (Brunauer, Emmett and Teller) analysis

N_2 adsorption-desorption isotherms were used to clarify specific surface textures and pore size of sample coded NAO-3 NPs. Results demonstrate *type IV*, which according to IUPAC classification, belongs to *type H3* hysteresis loop for relative pressure P/Po □ 0–1, as shown in Fig. 7(c). Low adsorption in low-pressure area and enhanced adsorption with expanding pressure are characteristics of *type IV* isotherms [69]. From BET surface area analysis, total pore volume, and average pore diameter are remarked to be 85.078 $m^2.g^{-1}$, 0.1704 $cm^3.g^{-1}$, and 8.0138 nm, correspondingly.

3.8.Electrocatalytic activity study

Electrocatalytic degradation of *Carmine* and *EY* dyes over N-doped δ-Al_2O_3 NPs catalyst was assessed under-maintained at ambient conditions and surrounding pressure with an applied potential (DC) of 10 V. To realize an adsorption/desorption equilibrium, catalyst-loaded solution of dye was maintained in dark environment for half an hour. For 12 minutes, solution was simultaneously exposed to a continuously applied current voltage to execute the electrocatalytic process of NAO NPs catalyst. Every two minutes, a sample was taken. The highest absorption of carmine dye can be seen at λ_{max} 518 nm, and EY dye at λ_{max} 515 nm. Degradation of these dyes in absence and existence of NAO NPs shows complete degradation in 10 min for *Carmine* dye and 12 min for electrocatalytic degradation, as shown in Figs. *S1* and *S2* (*Supplementary materials*). Decline of intensities of absorption band with NAO NPs under irradiation time was detected for *Carmine*. *EY* dyes revealed that nanocomposite NAO NPs effectively degraded dyes. The electrolysis of *Carmine* and *EY* dyes is 71.7% and 59.1%, while maximum electrocatalytic activity degradation of *Carmine* and *EY* dyes with NAO-3 NPs is 96.25% and 97.50%, respectively, as shown in Figs. 8(a, b).

3.8.1. Kinetic study

A kinetics study was applied to induce more quantitative understanding for electrocatalytic activity of NAO NPs. The *pseudo*-first-order kinetics produces the rate constant of electrocatalytic reaction based on *Eq. (9)*.

$$ln\left(\frac{A_t}{A_o}\right) = -kt, \quad \textbf{(9)}$$

Where, A_o, A_t, and K represents initial and absorbance, and kinetic constant at any point during the degradation process (min^{-1}); respectively [70]. Plotting was used to determine the rate

View Article Online
DOI: 10.1039/D6NA00277C

constant. $ln\left(\frac{A_t}{A_o}\right)$ as a function of time shows a linear correlation as presented in Figs. 8(c, d). The electrocatalytic behavior of fabricated NAO NPs catalyst was measured for varying incorporated gelatin content while maintaining a constant dye solution concentration. The rate constant k for *Carmine* and EY dyes is shown in Table 2. Rate constants were calculated as 0.28112 and 0.19828 min^{-1} with NAO-3 NPs for electrocatalytic degradation of *Carmine* and *EY* dyes, as shown in Fig. 8(e). NAO-3 NPs have high electrocatalytic activity, because introducing gelatin to δ-Al_2O_3 significantly reduces energy band gaps, and high surface area which readily absorb photons to increase final efficiency and improve electrocatalytic activity, compared to other reported findings in Table 3. N-doped metal oxide might also lower the energy band gap of aluminum oxide NPs. With abundant N atoms, gelatin is a perfect nitrogen precursor that improves characteristics of δ-Al_2O_3 NPs by raising the conductivity of aluminum oxide particles or lowering their contact resistance [71, 72]. Table 3 lists a comparison study for many used electrocatalysts for degradation efficiency of *Eosin yellow* and *Carmine* dyes.

Table 3: Comparison of different electrocatalysts for degradation efficiency of *E*osin yellow & *C*armine dyes.

Type of Catalyst	Method of preparation	Reaction condition							Ref.
		Dye	Dye Conc., (ppm)	Catalyst Conc., (g/l)	Electrolyte	Current Voltage, (V)	Time, (min)	Degradation (%)	
N- Fe_2O_3/G	Auto-Combustion method	IC	100	0.05	1 M NaCl	5	45	95.18	[73]
50% $BiOCl/TiO_2$	Microemulsion process	EY	50	1	0.10 M Na_2SO_4	-	120	93.6	[74]
graphite–ZnO NCs	Sol-gel method	EY	70	-	0.1 M Na_2SO_4	1.5	120	76	[75]
BaO/G	Auto-Combustion method	MB	10	0.05	1 M NaCl	10	25	97.1	[76]
NAO-3 NPs	Auto-Combustion method	Carmine EY	100 50	0.05	1 M NaCl	10	10 12	96.25 97.50	Present study

View Article Online
DOI: 10.1039/D6NA00277C

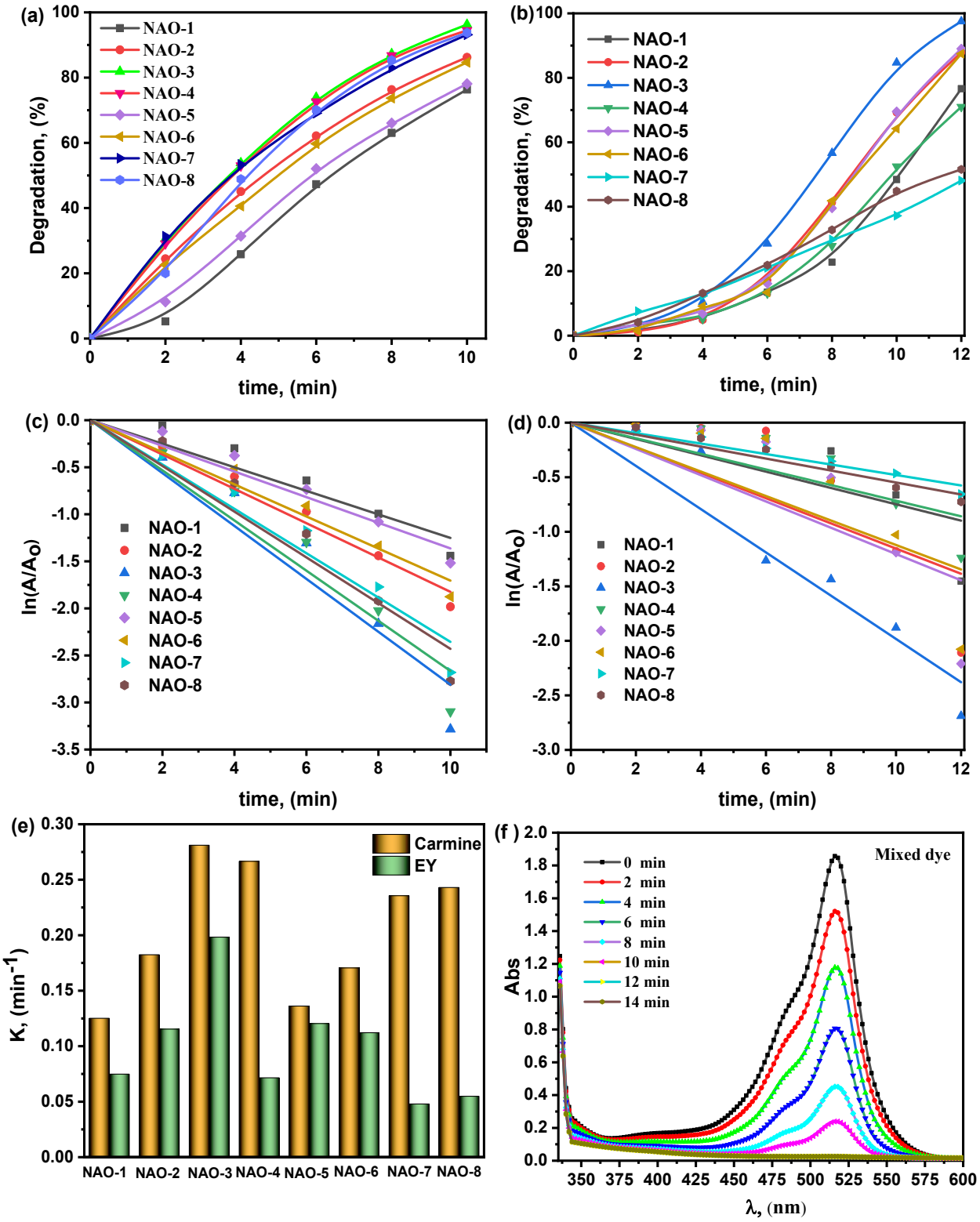

Fig. 8 (a, b) Degradation efficacy of Carmine and Eosin yellow dye, **(c, d)** kinetic rate of degradation, **(e)** constant rate of reaction of carmine and eosin yellow dye with different NAO NPs, and **(f)** UV–Vis. Spectrum of mixed dye with NAO-3 NPs.

View Article Online
DOI: 10.1039/D6NA00277C

3.8.2. Electrocatalytic degradation of mixed dyes

Figure 8(f) displays the range of two dye combinations (*Carmine* and *EY*) and shows degraded over time. The wavelength overlap for *EY* and *Carmine* at 516 nm is found to be the maximum absorbance value for each dye. Because of their similar π-conjugated electronic structures and anionic chromophores, *Carmine* and *EY* dyes absorb light in almost the same visible λ range, which causes spectral interference or a mixed color appearance [77, 78]. In the dye's degradation study, NAO-3 NPs electrocatalyst was chosen and applied for this test. After 14 minutes, there is a decrease in each dye's absorption intensity under electrocatalytic activity without complete degradation. The degradation of mixed dye is 98.60 %. Compared to anionic dye pollutants, NAO-3 NPs are more efficient in eliminating dyes because the surface of NAO-3 NPs contains Lewis's acid sites (Al^{3+} ions) that degrade these dyes. The results show that NAO-3 NPs electrocatalysts can be used efficiently in wastewater treatment.

3.8.3. Influence of radical scavengers' species

To investigate role of *ROS* in NAO-3 NPs electrocatalysts, active characters scavenger, which is responsible for photodegradation, Fig. 9(a). Ascorbic acid, isopropyl alcohol, ethylenediaminetetraacetic acid (*EDTA*), and sodium nitrate ($NaNO_3$) were previously used as radicals of $O_2^{-\bullet}$, $OH^{\bullet}$, h^+ and e^-, respectively, for EC reactions [79]. Degradation rate evidently reduced upon addition of exact trapping-scavengers to *carmine* dye from 96.3 % with NAO-3 NPs. This decrease in *Carmine* dye degradation is ascribed to exact trapping scavengers, which remove approximately 11.6%, 53.7%, 25.7% and 9.2% of *Carmine* dye, respectively. In Fig. 9(a) degradation efficiency of *Carmine* dye doesn't significantly decrease with addition of isopropyl alcohol and EDTA. Additionally, introduction of ascorbic acid and $NaNO_3$ affected substantial reduction in the degradation efficacy of *carmine* dye. These phenomena suggest the crucial roles of $O_2^{-\bullet}$ and e^- in degradation of *Carmine* dye.

3.8.4. Mechanism of electrocatalytic oxidation of Carmine dye degradation

The removal of pollutants through electrochemical oxidation can be achieved through direct anodic oxidation, which produces poor decontamination, or indirect oxidation, which is produced by molecules forming on the anode surface. These two processes can occur simultaneously or independently in a reactor [80]. In electrochemical oxidation, electrolytes such as sulfates, nitrates, perchlorates, and chlorides greatly improve electrical conductivity and lower energy consumption, which impacts the removal of contaminants and generation of active species. In contaminated

View Article Online
DOI: 10.1039/D6NA00277C

wastewater, chloride is a common electrolyte that produces active species such as active chlorine compounds to form chlorine gas (Cl_2), which is then reacted with water to make $HOCl$,but $HOCl$ then breaks down into hypochlorite ions (ClO^-), a powerful oxidant that responsible for dye degradation *via* reactions [81-83]:

$$2Cl^- \rightarrow Cl_2 + 2e^- \quad (Anode) \quad \textbf{(10)}$$

The hypochlorous acids release chlorine and then dissociate to produce the hypochlorite ion.

$$Cl_2 + H_2O \rightarrow H^+ + Cl^- + HOCl \quad \textbf{(11)}$$

$$HOCl \leftrightarrow H^+ + ClO^- \quad \textbf{(12)}$$

$$Dye + ClO^- \rightarrow Cl^- + CO_2 + H_2O \quad (Cathode) \quad \textbf{(13)}$$

Electrons in NAO-3 NPs is driven from the valence band to conduction band by an applied potential, producing free electrons (e^-) and holes (h^+). These electrons cause dissolved oxygen to transform into superoxide ($O_2^{\bullet -}$) radicals. First, electrons go through an external circuit during degradation processes, producing very reactive superoxide radicals. Our research has demonstrated that *Carmine* dye degradation on NAO-3 NPs is primarily caused by $O_2^{\bullet -}$ and e^- [84]. Interestingly, it is mainly $O_2^{\bullet -}$ that is liable for degrading *Carmine* dye on NAO-3 NPs, as shown in Fig. 9(a). The equations below describe formation of active species on catalyst surface [85]:

$$O_2 + e^- \rightarrow O_2^{\bullet -} \quad \textbf{(14)}$$

$$O_2^{\bullet -} + H_2O \rightarrow OH^- + HO_2^{\bullet} \quad \textbf{(15)}$$

$$HO_2^{\bullet} + H^+ \rightarrow OH^- + OH^{\bullet} \quad \textbf{(16)}$$

$$OH^- + h^+ \rightarrow OH^{\bullet} \quad \textbf{(17)}$$

$$OH^{\bullet} + Carmine\ dye \rightarrow CO_2 + H_2O + other\ product \quad \textbf{(18)}$$

3.8.5. Reusability and stability

For real-world uses, the electrocatalyst's stability is crucial, where five cycle tests were conducted using the same experimental setup for ten minutes of exposure to the applied voltage to examine stability of NAO-3 NPs. Centrifugation was used to collect the catalyst after each cycling experiment, and it was then cleaned with distilled water for use in the subsequent run. For real-world uses, the electrocatalyst's stability and reusability are crucial. Figure 9(b) illustrates how NAO-3 NPs degrade carmine dye; after five cycles of electrocatalytic degradation, NAO-3 NPs' electrocatalytic performance decreases slightly from 96.25 % to 90.5 %. Demonstrating the NAO-3 NPs' excellent stability and recyclability throughout the electrocatalytic reaction process.

View Article Online
DOI: 10.1039/D6NA00277C

Additionally, the loss might be unavoidable of electrocatalyst weight during washing and centrifugation may be responsible for the small decline in electrocatalytic performance. The structure stability of NAO-3 NPs after five cycles was studied using XRD and FTIR analysis. The Fig. 9(c) shows that no obvious shift comparative to XRD patterns of fresh NAO-3 NPs in characteristic's diffraction peaks was compared to fresh sample, indicating crystalline structure remains after repeatable cycle. While a notice slight decrease in intensity of XRD peaks is due to reducing in crystallinity or exposure of active planes after recycle [86]. Figure 9(d) shows FTIR that absorption of water is responsible for the broad band absorption at ν 3422cm^{-1} [87].

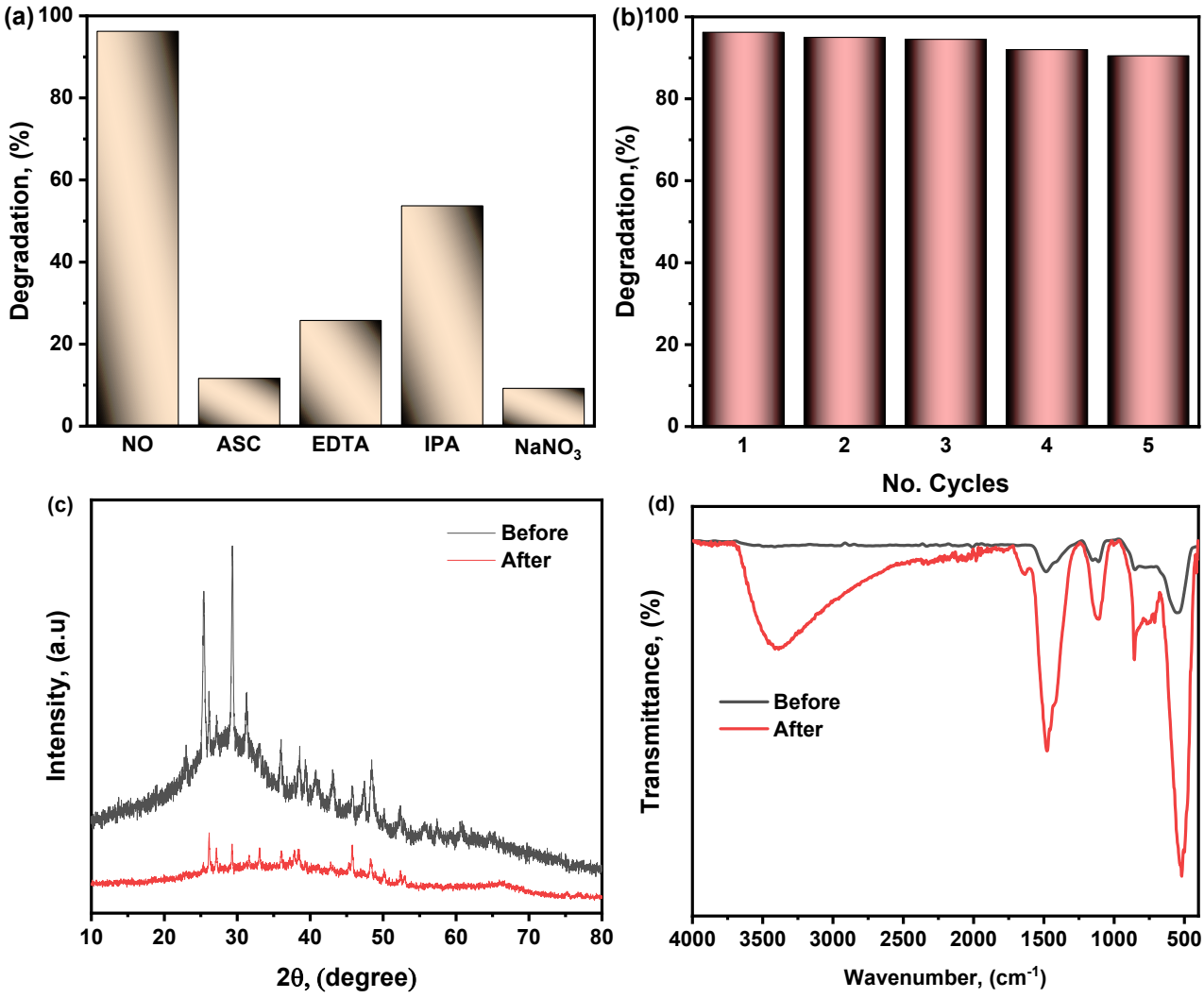

Fig. 9 (a) Electrocatalytic degradation in presence of NaCl and different scavengers for *Carmine* dye, **(b)** EC degradation of *Carmine* dye for five runs, **(c)** XRD patterens, and **(d)** FTIR spectra after reusability,

View Article Online
DOI: 10.1039/D6NA00277C

4. Conclusions

A novel N-doped δ-Al_2O_3 NPs was fabricated by sol-gel/auto-combustion method, where gelatin was incorporated as a source for N-doping onto δ-Al_2O_3 NPs. The phase structure, chemical structure, and morphological/elemental analysis were verified using different instrumented characterizations. In DRS analysis, gelatin to δ-Al_2O_3 reduces energy band gaps. Thus, N-doped δ-Al_2O_3 NPs are used to study electrocatalytic activity for the degradation of *Carmine, Eosin yellow*, and mixed dyes. The chosen NAO-3 NPs catalyst achieved notably the degradation efficiency of 96.25%, 97.5%, and 98.60% with (10, 12, and 14 min) for *Carmine, Eosin yellow*, and mixed dyes, respectively. The reactive species responsible for *Carmine* dye degradation showed that it is mainly $O_2^{\bullet-}$ and *HOCl* with H_2O and Cl^- oxidation to Cl_2 as a primary oxidizing agent responsible for degrading *Carmine* dye on NAO-3 NPs. After assessing the results, the chosen and preferred NAO-3 NPs catalyst showed good efficiency and recyclability following rescue cycles.

Declarations

Acknowledgment: All authors acknowledge "the Deanship of Scientific Research, Vice Presidency for Graduate Studies and Scientific Research, King Faisal University, Saudi Arabia [Project No. KFU260554], for financial support.

Competing interests: The authors declare that they have no known competing financial interests or personal relationships that could have appeared to influence the work reported in this paper.

Ethical Approval: This article does not contain any animal studies by the authors.

Authors' contributions: Ahmed T. Mosleh, H.Y. Zahran and **Tarek A. Yousef**: Methodology, formal analysis, and data curation. **Habiba A. Hossni, Nourhan A. M Ragab**: Resources, data optimization, software, data analysis. **Mohamed Hafez** and **Shereef A. Fareed**: Resources and Project management. **Elbadawy A. Kamoun,** and **Ibrahim S. Yahia**: Project management, supervision, wrote the original draft and reviewed the final draft. All authors approved the current and final version of the manuscript for submission.

Data availability: All data is available in the manuscript and is available when requested by the corresponding author.

Funding statement: This work was supported by "the Deanship of Scientific Research, Vice Presidency for Graduate Studies and Scientific Research, King Faisal University, Saudi Arabia [Project No. KFU260554].

References

1. Zhou X, Yang J, Guo J, Xiong W, Leung MKH. Advances and Prospects in Electrocatalytic Processes for Wastewater Treatment. Processes. 2024; 12(8).
2. Mishra S, Sundaram B. A review of the photocatalysis process used for wastewater treatment. Materials Today: Proceedings. 2024. **102**, 393-409.
3. Sağlam S, Türk FN, Arslanoğlu H. Use and applications of metal-organic frameworks (MOF) in dye adsorption: Review. Journal of Environmental Chemical Engineering. 2023. **11**, 11056.
4. Alvi M, Batstone D, Mbamba CK, Keymer P, French T, Ward A, et al. Deep learning in wastewater treatment: a critical review. Water Research. 2023. **245**, 120518.
5. Kumari H, Sonia, Suman, Ranga R, Chahal S, Devi S, et al. A Review on Photocatalysis Used For Wastewater Treatment: Dye Degradation. Water, Air, & Soil Pollution. 2023. **234**, 349.

View Article Online
DOI: 10.1039/D6NA00277C

6. Panhwar A, Sattar Jatoi A, Ali Mazari S, Kandhro A, Rashid U, Qaisar S. Water resources contamination and health hazards by textile industry effluent and glance at treatment techniques: A review. Waste Management Bulletin. 2024. **1**, 158-63.
7. Song Y, Wang L, Qiang X, Gu W, Ma Z, Wang G. An overview of biological mechanisms and strategies for treating wastewater from printing and dyeing processes. Journal of Water Process Engineering. 2023. **55**, 104242.
8. Rani SLS, Satyannarayana KVV, Arthanareeswaran G, Raja VK. Treatment of food processing industries wastewaters using a new clay-based inorganic membrane: Performance evaluation and fouling analysis. Journal of the Taiwan Institute of Chemical Engineers. 2025.**166**, 105439.
9. Wani AA, Rather RA, Shaari N, Khan U, Muhammad T, Hussain SM, et al. Aspects of superior photocatalytic dye degradation and adsorption efficiency of reduced graphene oxide multiwalled carbon nanotubes with modified ZnO-Al_2O_3 nanocomposites. Journal of Environmental Chemical Engineering. 2024. **12**, 112461.
10. El-Sayed F, Hussien MSA, AlAbdulaal TH, Abdel-Aty A-H, Zahran HY, Yahia IS, et al. Study of catalytic activity of G-SrO nanoparticles for degradation of cationic and anionic dye and comparative study photocatalytic and electro & photo-electrocatalytic of anionic dye degradation. Journal of Materials Research and Technology. 2022. **20**, 959-75.
11. Mosleh AT, Kamoun EA, El-Moslamy SH, Salim SA, Zahran HY, Zyoud SH, et al. Performance of Ag-doped CuO nanoparticles for photocatalytic activity applications: Synthesis, characterization, and antimicrobial activity. Discover Nano. 2024. **19**, 16.
12. den Uijl MJ, Lokker A, van Dooren B, Schoenmakers PJ, Pirok B, van Bommel MR. Comparing different light-degradation approaches for the degradation of crystal violet and eosin Y. Dyes and Pigments. 2022. **197**, 109882.
13. Pierau L, Abbad Andaloussi S, Chiappone A, Lajnef S, Peyrot F, Malval J-P, et al. Eosin Y derivatives for visible light-mediated free-radical polymerization: Applications in 3D-photoprinting and bacterial photodynamic inactivation. European Polymer Journal. 2024. **214**, 113143.
14. Hu L, Li M, Cheng L, Jiang B, Ai J. Solvothermal synthesis of octahedral and magnetic $CoFe_2O_4$–reduced graphene oxide hybrids and their photo-Fenton-like behavior under visible-light irradiation. RSC Advances. 2021. **11**, 22250-63 D.
15. Mosleh AT, Al-Harbi FF, Gouadria SM, Zyoud SH, Zahran HY, Hussien MSA, et al. Photodegradation of Wastewater Containing Organic Dyes Using Modified G-C_3N_4-Doped ZrO_2 Nanostructures: Towards Safe Water for Human Beings. Catalysts. 2024; 14(1).
16. Raza Q, Fatima G, Altilasi HH, Aldosari E, Hussain I, Hossain MA, et al. Superior photocatalytic behaviour of MnFe2O4@TiO2@MWCNTs hybrid photocatalyst for efficacious degradation of enrofloxacin antibiotic from veterinary wastewater. International Journal of Environmental Science and Technology. 2025. **23**, 143.
17. Sharma S, Devi A, Bhattacharyya KG. Nickel-titanium dioxide-Fuller's earth nanocomposites: Synthesis, characterization and application as a photocatalyst in aqueous methylene blue degradation under visible light irradiation. Inorganic Chemistry Communications. 2023. **151**, 110550.
18. Fatima G, Firdous S, Raza Q, Aamir M, Alsaikhan K, Khezami L, et al. High surface area Gd/Mn co-doped LaFeO3 CNT photocatalyst with superior solar amoxicillin degradation and recyclability across wide pH range.Surfaces and Interfaces.2026. **89**, 109165.
19. Xin S, Huo S, Zhang C, Ma X, Liu W, Xin Y, et al. Coupling nitrogen/oxygen self-doped biomass porous carbon cathode catalyst with CuFeO2/biochar particle catalyst for the heterogeneous visible-light driven photo-electro-Fenton degradation of tetracycline. Applied Catalysis B: Environmental. 2022. **305**, 121024.
20. Prakash Kushwaha J, Chandra Srivastava V, Deo Mall I. Studies on electrochemical treatment of dairy wastewater using aluminum electrode. AIChE Journal. 2011. **57**, 2589-98.

View Article Online
DOI: 10.1039/D6NA00277C

21. Singh S, Srivastava VC, Mall ID. Multistep Optimization and Residue Disposal Study for Electrochemical Treatment of Textile Wastewater Using Aluminum Electrode. **11**, 31-4.
22. Jun B-M, Nam S-N, Jung B, Choi JS, Park CM, Choong CE, et al. Photocatalytic and electrocatalytic degradation of bisphenol A in the presence of graphene/graphene oxide-based nanocatalysts: A review. Chemosphere. 2024. **356**, 141941.
23. Liu Y, Wu J, Li X, Chen J, Li Y, Luo X, et al. Highly efficient $CoTiO_3$/MOF-derived In_2S_3 photo-electrocatalysts: Degradation kinetics, pathways, and mechanism. Journal of Alloys and Compounds. 2024. **975**, 172921.
24. Pillai IMS, Gupta AK. Batch and continuous flow anodic oxidation of 2,4-dinitrophenol: Modeling, degradation pathway and toxicity. Journal of Electroanalytical Chemistry. 2015. **756**, 108-17.
25. Sasidharan Pillai IM, Gupta AK. Potentiostatic electrodeposition of a novel cost effective PbO_2 electrode: Degradation study with emphasis on current efficiency and energy consumption. Journal of Electroanalytical Chemistry.2015. **749**, 16-25.
26. Sirés I, Brillas E, Oturan MA, Rodrigo MA, Panizza M. Electrochemical advanced oxidation processes: today and tomorrow. A review. Environmental Science and Pollution Research. 2014. **21**, 8336-67.
27. Li Y, Bu J, Sun Y, Huang Z, Zhu X, Li S, et al. Efficient degradation of norfloxacin by synergistic activation of PMS with a three-dimensional electrocatalytic system based on Cu-MOF. Separation and Purification Technology.2025. **356**, 129945.
28. Xu H, Sun X, Yang H, Cui J, Wang J, Kang Y, et al. Degradation of aqueous phenol by combined ultraviolet and electrochemical oxidation treatment. Journal of Cleaner Production. 2024. **436**, 140672.
29. Jiang S, Zhang Q, Cheng S, Liu J, Fu X, Shang S, et al. Rich oxygen vacancies 2D-nanoholey NiCo2O4-δ for selective and stable methane electrooxidation to acetaldehyde. Journal of Energy Chemistry.2026. **116**, 843-53.
30. Rajendran S, Palani G, Shanmugam V, Trilaksanna H, Kannan K, Nykiel M, et al. A Review of Synthesis and Applications of Al_2O_3 for Organic Dye Degradation/Adsorption. Molecules. 2023; 28(23).
31. Almomani F, Al-Rababah A, Tawalbeh M, Al-Othman A. A comprehensive review of hydrogen generation by water splitting using 2D nanomaterials: Photo vs electro-catalysis.Fuel.2023. **332**, 12590.
32. Yang C, Li X-y, Lin L. Fabrication of a SnO_2-Sb nano-pin array anode for efficient electrocatalytic oxidation of bisphenol A in wastewater.Journal of Hazardous Materials.2023. **444**, 130444.
33. Guo Y, Wu S, La P, Zhou D, Ji Z, Wang X. 3D-printing advanced ZIF-67@aluminum phosphate/Al_2O_3 ceramic catalyst by aluminum phosphate-assisted surface bonding. Mater. Sci. Addit. Manuf 2025. **4**.
34. Yasin Ahmed T, Aziz SB, M. A. Dannoun E. New photocatalytic materials based on alumina with reduced band gap: A DFT approach to study the band structure and optical properties. Heliyon. 2024. **10**.
35. Nagarajan P, Subramaniyan V, Elavarasan V, Mohandoss N, Subramaniyan P, Vijayakumar S. Biofabricated Aluminium Oxide Nanoparticles Derived from Citrus aurantium L.: Antimicrobial, Anti-Proliferation, and Photocatalytic Efficiencies. Sustainability. 2023; 15(2).
36. Raza Q, Fatima G, Lu B, Bibi I, An J, Lim S. In-situ synthesis and synergistic effect of Ag/Al@SrFe12O19 decorated with graphitic carbon nitride: mechanistic insight of photocatalytic and antimicrobial susceptibility. Surfaces and Interfaces.2025. **72**, 107203.
37. Congreve RC, Quezada CP, Kokkarachedu V. Aluminum Oxide Nanoparticles: Properties and Applications Overview. In: Kokkarachedu V, Sadiku R, editors. Nanoparticles in Modern Antimicrobial and Antiviral Applications. Cham: Springer International Publishing; 2024. 265-88.
38. Orooji Y, Mohassel R, Amiri O, Sobhani A, Salavati-Niasari M. Gd_2ZnMnO_6/ZnO nanocomposites: Green sol-gel auto-combustion synthesis, characterization and photocatalytic degradation of different dye pollutants in water. Journal of Alloys and Compounds.2020. **835**, 155240.

View Article Online
DOI: 10.1039/D6NA00277C

39. Sacco O, Mancuso A, Venditto V, Pragliola S, Vaiano V. Behavior of N-Doped TiO_2 and N-Doped ZnO in Photocatalytic Azo Dye Degradation under UV and Visible Light Irradiation: A Preliminary Investigation. Catalysts. 2022; 12(10).
40. Manikandan V, Jayanthi P, Priyadharsan A, Vijayaprathap E, Anbarasan PM, Velmurugan P. Green synthesis of pH-responsive Al_2O_3 nanoparticles: Application to rapid removal of nitrate ions with enhanced antibacterial activity.Journal of Photochemistry and Photobiology A: Chemistry. 2019. **371**, 205-15.
41. Pang YL, Tee SF, Limg S, Abdullah AZ, Ong HC, Wu C-H, et al. Enhancement of photocatalytic degradation of organic dyes using ZnO decorated on reduced graphene oxide (rGO).Desalination and Water Treatment.2018. **108**, 311-21.
42. Ghozza MH, Yousef TA, Al-Dakhil A, Ferjani H, Alosaimi AM, Abdel-Hameed R, et al. Exploring the electrical and magnetic characteristics of novel barium-doped bismuth ferrite ($Bi_{0.9}Ba_{0.1}FeO_3$) nanocomposites and their applications for electrocatalytic degradation of Congo red dye. RSC Advances. 2025. **15**, 10970-83.
43. Xu J, Lu Y, Zhao D, Du D, Song J. Synergistic enhancement of visible-light photocatalysis in X/Fe_3O_4/AlON heterojunctions for efficient and recoverable dye degradation. Ceramics International. 2026. **52**, 2643-53.
44. Khorsand Zak A, Esmaeilzadeh J, Hashim AM. Exploring the gelatin-based sol-gel approach: A convenient route for fabricating high-quality pure and doped ZnO nanostructures.Ceramics International.2024. **50**, 12649-6.
45. Liu W, Ai Z, Zhang L. Design of a neutral three-dimensional electro-Fenton system with foam nickel as particle electrodes for wastewater treatment.Journal of Hazardous Materials. 2012. **243**, 257-6.
46. Teng X, Li J, Wang Z, Wei Z, Chen C, Du K, et al. Performance and mechanism of methylene blue degradation by an electrochemical process. RSC Advances. 2020. **10**, 24712-20.
47. Lippens B, De Boer. Study of phase transformations during calcination of aluminum hydroxides by selected area electron diffraction. Acta Crystallographica, 1964. **17**, 1312-21.
48. Peiris S, Jayasundera. Synthesis, Characterization and Phase Transition of Highly Porous γ-Alumina Nanoparticles. International Journal for Research in Applied Sciences and Biotechnology. 2020.
49. Vinothkumar P, Manoharan C, Shanmugapriya B, Bououdina M. Effect of reaction time on structural, morphological, optical and photocatalytic properties of copper oxide (CuO) nanostructures.Journal of Materials Science: Materials in Electronics. 2019. **30**, 6249-62.
50. Zhou S, Antonietti M, Niederberger M. Low-Temperature Synthesis of γ-Alumina Nanocrystals from Aluminum Acetylacetonate in Nonaqueous Media. Small.2007. **3**, 763-7.
51. Qadir M, Hossan J, Gafur M, Karim M. Preparation and Characterization of Gelatin-Hydroxyapatite Composite for Bone Tissue Engineering. International Journal of Engineering & Technology Sciences.2014. **14**, 24.
52. Das M, R S, Prasad K, Jv V, M R. Extraction and characterization of gelatin: a functional biopolymer.International Journal of Pharmacy and Pharmaceutical Sciences.2017. **9**, 239.
53. Gharbi AH, Laouini SE, Hemmami H, Bouafia A, Gherbi MT, Ben Amor I, et al. Eco-Friendly Synthesis of Al2O3 Nanoparticles: Comprehensive Characterization Properties, Mechanics, and Photocatalytic Dye Adsorption Study. Coatings. 2024; 14(7).
54. Rabu R, Jewena N, Das SK, Khandaker J, Ahmed F. Synthesis of Metal-Oxide (Al_2O_3) Nanoparticles by using Autoclave for the Efficient Absorption of Heavy Metal Ions. Journal of Nanomaterials & Molecular Nanotechnology. 2020. **9**, 1-6.
55. Deshmukh K, Ahamed MB, Deshmukh RR, Pasha SKK, Sadasivuni KK, Polu AR, et al. Newly developed biodegradable polymer nanocomposites of cellulose acetate and Al_2O_3 nanoparticles with enhanced dielectric performance for embedded passive applications. Journal of Materials Science: Materials in Electronics. 2017. **28**, 973-86.

View Article Online
DOI: 10.1039/D6NA00277C

56. Vural S, Sari Ö. Synthesis and characterization of SDS assistant α-alumina structures and investigation of the effect of the calcination time on the morphology. Colloid and Polymer Science.2019. **297**, 107-14.
57. Shuai X, Zeng Y, Li P, Chen J. Fabrication of fine and complex lattice structure Al2O3 ceramic by digital light processing 3D printing technology. Journal of Materials Science. 2020. **55**, 6771-8.
58. Mohammed AA, Khodair ZT, Khadom AA. Preparation and investigation of the structural properties of α-Al2O3 nanoparticles using the sol-gel method. Chemical Data Collections. 2020. **29**, 100531.
59. Tadic M, Kralj S, Kopanja L. Synthesis, particle shape characterization, magnetic properties and surface modification of superparamagnetic iron oxide nanochains. Materials Characterization. 2019. **148**, 123-33.
60. Mohamad SNS, Mahmed N, Halin DSC, Razak KA, Norizan MN, Mohamad IS. Synthesis of alumina nanoparticles by sol-gel method and their applications in the removal of copper ions (Cu^{2+}) from the solution.IOP Conference Series: Materials Science and Engineering. 2019. **701**, 012034.
61. Gholizadeh Z, Aliannezhadi M, Ghominejad M, Tehrani FS. High specific surface area γ-Al2O3 nanoparticles synthesized by facile and low-cost co-precipitation method. Scientific Reports. 2023. **13**, 6131.
62. Hai C, Zhang G, Liu J, Zhou Y, Dong S, Zeng J, et al. ζ-potential variations of micro-nano sized hexagram-like α-Al2O3 particles. Journal of Nanoparticle Research.2020. **22**, 65.
63. Lai S-H, Chen Y-B, Li N, Su H, Guo S-H. Novel g-C_3N_4 wrapped γ-Al_2O_3 microspheres heterojunction for efficient photocatalytic application under visible light irradiation. Journal of Materials Science: Materials in Electronics.2018. **29**, 4509-16.
64. Nguyen DTC, Le HTN, Nguyen TT, Nguyen TTT, Bach LG, Nguyen TD, et al. Multifunctional ZnO nanoparticles bio-fabricated from Canna indica L. flowers for seed germination, adsorption, and photocatalytic degradation of organic dyes. Journal of Hazardous Materials. 2021. **420**, 126586.
65. Akouibaa A, Masrour R, Jabar A, Benhamou M, Ouarch M, Derouiche A. Study of the Optical and Thermoplasmonics Properties of Gold Nanoparticle Embedded in Al_2O_3 Matrix. Plasmonics.2022. **17**, 1157-69.
66. Akouibaa A, Masrour R, Abderrahim J, Benhamou M, Ouarch M, Derouiche A. Study of the Optical and Thermoplasmonics Properties of Gold Nanoparticle Embedded in Al_2O_3 Matrix. Plasmonics. 2022. **17**, 1157-69.
67. Raza W, Haque MM, Muneer M, Bahnemann D. Synthesis of visible light driven TiO_2 coated carbon nanospheres for degradation of dyes.Arabian Journal of Chemistry.2019. **12**, 3534-45.
68. Singh KRB, Singh P, Singh J, Pandey SS. Nanobioengineered Al_2O_3 Core–Shell Nanoparticle Preparation Using Bauhinia Variegate Plant Extract for Efficient Photocatalysis and Electrochemical Sensing. ACS Applied Bio Materials. 2024. **7**, 7646-58.
69. Bekele EA, Korsa HA, Desalegn YM. Electrolytic synthesis of γ-Al_2O_3 nanoparticle from aluminum scrap for enhanced methylene blue adsorption: experimental and RSM modeling. Scientific Reports. 2024. **14**, 16957.
70. B A, A J, Rao AS, Nagarkar SS, Dutta A, Duttagupta SP, et al. Challenges in photocatalytic hydrogen evolution: Importance of photocatalysts and photocatalytic reactors.International Journal of Hydrogen Energy. 2024. **81**, 1442-66.
71. Abhishek B, Jayarama A, Rao AS, Nagarkar SS, Dutta A, Duttagupta SP, et al. Challenges in photocatalytic hydrogen evolution: Importance of photocatalysts and photocatalytic reactors. International Journal of Hydrogen Energy. 2024. **81**, 1442-66.
72. Mazouzi DE, Djani F, Soukeur A, Bouchal W, Manseri A, Derkaoui K, et al. Auto-combustion designed $BiFeO_3/Bi_2O_3$ photocatalyst for improved photodegradation of nitrobenzene under visible light and sunlight irradiation. Surfaces and Interfaces. 2024. **44**, 103581.

View Article Online
DOI: 10.1039/D6NA00277C

73. Mosleh AT, Hamad AA, Kamoun EA, Sheha E, Ganesh V, Abdel-Aty M, et al. A Novel eco-friendly synthesis of N-doped α-Fe_2O_3/graphene nanocomposites for enhanced electrocatalysis, photo/electrocatalysis degradation of organic dyes, and supercapacitance activity performance. Materials Chemistry and Physics: Sustainability and Energy. 2026. **6**, 100052.
74. Liu Z, Xu X, Fang J, Zhu X, Li B. Synergistic Degradation of Eosin Y by Photocatalysis and Electrocatalysis in UV Irradiated Solution Containing Hybrid BiOCl/TiO_2 Particles.Water, Air, & Soil Pollution.2012. **223**, 2783-98.
75. Ntsendwana B, Sampath S, Mamba BB, Oluwafemi OS, Arotiba OA. Photoelectrochemical degradation of eosin yellowish dye on exfoliated graphite–ZnO nanocomposite electrode. Journal of Materials Science: Materials in Electronics.2016. **27**, 592-.
76. Hussien MSA, Mosleh AT, Kamoun EA, Ganesh V, Al-Arjan WS, Zahran HY, et al. One-pot synthesis of BaO/Graphene nanocomposites for photo-electrocatalysis degradation of organic dye: A novel approach and nanocomposite performance assessment. Journal of Water Process Engineering. 2025. **79**, 108873.
77. Liu Q, He Z, Zeng M, Qin F, Wang Z, Liu G, et al. Effects of different food ingredients on the color and absorption spectrum of carminic acid and carminic aluminum lake. Food Science & Nutrition. 2021. **9**, 36-43.
78. Roy SC, Mahmood AJ. Effect of pH on Homogeneous Photodegradation of Eosin Y Dye.Journal of Nepal Chemical Society.2021. **42**, 1-.
79. Umadevi M, Rathinam R, Brindha T, Dheenadhayalan S, Pattabhi S. Application of Electro-Chemical Oxidation for the Treatment of Reactive Red 195 using Graphite Electrode. Asian Journal of Biological and Life Sciences. 2021. **10**, 620-5.
80. Fu R, Zhang P-S, Jiang Y-X, Sun L, Sun X-H. Wastewater treatment by anodic oxidation in electrochemical advanced oxidation process: Advance in mechanism, direct and indirect oxidation detection methods. Chemosphere. 2023. **311**, 136993.
81. Fu R, Zhang P-S, Jiang Y-X, Sun L, Sun X-H. Wastewater treatment by anodic oxidation in electrochemical advanced oxidation process: Advance in mechanism, direct and indirect oxidation detection methods. Chemosphere.2023. **311**, 136993.
82. Kamoun EA, Mokhtar AM, El-Khouly AS, Abu-Khudir R, Nassar MY, Ganesh V, et al. Novel hybrid nanocomposite based on Z-Scheme g-C_3N_4@Ag–$NiFe_2O_4$ for electrocatalytic degradation performance of organic dyes, and it's in vitro cytotoxicity assessment. Materials Chemistry and Physics. 2026. **356**, 132318.
83. Liu Y, Wang H, Ma H, Li Z, Liu L, Li Y, et al. Achieving the trifecta in industrial wastewater remediation: A compact stacked bioelectrochemical reactor with a Ni@UiO-66/GO cathode for concurrent energy recovery, metal reclamation, and organic mineralization. Separation and Purification Technology. 2026. **395**, 137927.
84. El-Sayed F, Hussien MSA, AlAbdulaal TH, Ismail A, Zahran HY, Yahia IS, et al. Comparative Degradation Studies of Carmine Dye by Photocatalysis and Photoelectrochemical Oxidation Processes in the Presence of Graphene/N-Doped ZnO Nanostructures. Crystals. 2022; 12(4).
85. Abdel-Megid M, Eissa ME, Mosleh AT, Ragab NAM, Zahran HY, Yahia IS, et al. Magnetic, electrical, and dielectric properties of microwave-assisted synthesis of $Bi_{0.6}Sr_{0.4}$ FeO_3 nanoparticles for wastewater treatments: Electro-degradation of Rhodamine B dye. Ceramics International. 2025. **51**, 39677-87.
86. Akram N, Guo J, Ma W, Guo Y, Hassan A, Wang J. Synergistic Catalysis of $Co(OH)_2$/CuO for the Degradation of Organic Pollutant Under Visible Light Irradiation. Scientific Reports. 2020. **10**, 193.
87. Luong NT, Hanna K, Boily J-F. Water film-mediated photocatalytic oxidation of oxalate on TiO_2. Journal of Catalysis. 2024. **432**, 115425.

View Article Online
DOI: 10.1039/D6NA00277C

Data Availability Statement

The data sets used and/or analyzed during the current study are available from the corresponding authors upon reasonable request.